

Stationary flux ropes at the southern terminator of Mars

M. J. Beharrell¹ and J. A. Wild¹

Received 19 March 2012; revised 14 September 2012; accepted 14 October 2012; published 11 December 2012.

[1] Flux ropes have long been observed in the upper atmosphere of Venus and more recently at Mars. Here we present magnetic field measurements of flux ropes encountered at the southern terminator of Mars by Mars Global Surveyor and compare them to a flux rope model. This allows several parameters of each rope to be inferred. Remarkably similar flux ropes are met repeatedly at the southern terminator over a period of the Martian year, when strong crustal magnetic fields are upstream of their position, indicating that they are most likely stationary and attached to the upstream crustal fields. A mechanism is described that could produce the observed flux ropes.

Citation: Beharrell, M. J., and J. A. Wild (2012), Stationary flux ropes at the southern terminator of Mars, *J. Geophys. Res.*, *117*, A12212, doi:10.1029/2012JA017738.

1. Introduction

[2] Flux ropes are common in a range of different space plasmas contexts. For example, they occur in the day side ionosphere of Venus [e.g., Russell, 1990], in the solar corona [e.g., Petrie, 2007], and in the vicinity of Earth's magnetopause [e.g., Hasegawa *et al.*, 2006; Elphic and Southwood, 1987]. In the atmosphere of the Sun, as magnetic flux escapes the Solar chromosphere to form twisted structures in the corona, it settles in to the minimum energy configuration: the flux rope. It is not a potential state (i.e., current free) everywhere because the helicity of the twisted field must be conserved. Instead it is a long, thin filament of highly twisted magnetic field, along which currents may flow either parallel or anti-parallel to the magnetic field direction.

[3] As spacecraft pass close to, or through, flux ropes, on board magnetometers can detect their presence as rotations in the magnetic field. Recently, magnetic signatures typical of large, high intensity flux ropes have been reported near the southern terminator of Mars [Brain *et al.*, 2010], and later confirmed by multispacecraft measurements [Morgan *et al.*, 2011]. Occurrences of these strong (>100 nT) flux ropes are reportedly common, having been identified by Brain *et al.* [2010] in ~1% of Mars Global Surveyor (MGS) orbits. The largest of these occurred at 04:55 UT on 9 March 2002. In terms of its magnetic field strength, it is thought to be the greatest flux rope measured in situ to date anywhere in the solar system. At the time of the measurement, MGS was positioned far from any significant crustal magnetic field sources. While not ruling out the possibility of the flux rope being stationary, Brain *et al.* [2010] argued that it could be traveling with the surrounding plasma flow, which is

typically 5 km s⁻¹ to 15 km s⁻¹. In this paper we present evidence that the large flux rope of 9 March 2002 is a class of stationary flux rope that appear with specific orientations of the planet.

2. Instrumentation

[4] Following the work of Brain *et al.* [2010], we revisit the magnetometer and electron reflectometer (MAG/ER) data set from the Mars Global Surveyor spacecraft. In March 1999, MGS entered the mapping phase of its mission. This was a near 2:00 am / 2:00 pm sun-synchronous orbit, with an altitude ranging from 368 km to 438 km above the surface. After 88 orbits, and 7 Martian solar days, the spacecraft retraces its path, with a small offset to the East of 58.6 km when measured at the equator. The mapping phase was envisaged to last one Martian year (687 days), but following an extension, the mission finally ended in November 2006. Processed data available from the NASA Planetary Data System include magnetometer measurements in Mars Solar Orbital (MSO) coordinates, at 0.75 s resolution (dropping to 1.5 s or 3 s, depending on telemetry allocation), and electron flux densities, at 2 s, 4 s, or 8 s resolution, with 19 energy channels spanning 10 eV to 20 keV. The data are provided in physical units, and instrumental and spacecraft effects have been removed during the processing stage.

3. Observations

[5] Figure 2 shows the magnetic field in MSO coordinates during five intervals of interest. The solid lines are measurements from MGS, and the dashed lines are values from the Cain *et al.* [2003] crustal magnetic field model. The panels each contain data from a consecutive pass through the southern terminator region, separated by 88 orbits (approximately one week). Unfortunately, data does not exist for the pass between those marked "example A" and "example B".

[6] Example A is the large flux rope of 9 March 2002, previously discussed by Brain *et al.* [2010]. The arrow in the center of the plot marks the point of maximum magnetic field

¹Department of Physics, Lancaster University, Lancaster, UK.

Corresponding author: M. J. Beharrell, Department of Physics, Lancaster University, Lancaster LA1 4YB, UK.
(m.bharrell@lancaster.ac.uk)

©2012. American Geophysical Union. All Rights Reserved.
10.1029/2012JA017738

strength, $|\mathbf{B}|_{\max}$, and the text indicates the corresponding solar longitude (L_S), location in planetary coordinates, and solar zenith angle (SZA). Solar longitude is the position of Mars in its orbit around the sun: 0° solar longitude is the northern hemisphere spring equinox, 90° is northern hemisphere summer solstice, and so on. The data in each of the other panels are aligned such that the arrow in the center of each plot marks the closest position, in MSO coordinates, to the location of $|\mathbf{B}|_{\max}$ during flux rope example A.

[7] A similar flux rope signature is seen in all of the panels. They share a fixed position in MSO coordinates, while the changing season means that the location of the flux ropes in planetary coordinates shifts over time. If there had not been a shift in planetary position, the signatures might have been mistakenly included in the empirical crustal magnetic field model, assuming the signals are present in a significant number of MGS orbits. The flux ropes are encountered at a solar zenith angle of around 93.8° , just beyond the terminator. The corresponding planetary latitudes range from -70.9° in the first observation, to -79.0° in the last.

[8] The variation in $|\mathbf{B}|$ between successive flux ropes is unlikely to be due to the small eastward displacement between the respective orbits, which is only around 10 km at this co-latitude, compared to the ~ 500 km size of the encounters along direction of the spacecraft's path. It is more likely that the magnetic field magnitude is changing with the orientation of the planet, and/or the prevailing solar wind conditions. If the flux ropes are breaking away and reforming, which we suspect occurs at least with each daily rotation of the planet, this could also explain the variation in magnitude between the observations.

4. Model Flux Rope

[9] The similarities between all flux rope signatures in Figure 2 strongly suggest that they are relatively static, and not transient or moving with the local plasma velocity. For this reason it is reasonable to neglect temporal variations, and begin a model with three of the equations governing a magnetic field in static equilibrium ($\partial/\partial t = 0$). The first to construct such a model, including both the internal and external magnetic fields, were *Gold and Hoyle* [1960]. Here we follow their assumptions, namely that the curvature of the flux rope is small enough to consider the section straight; the static flux ropes must be largely force-free, otherwise rapid motions would immediately be developed; and there is azimuthal symmetry of the magnetic field around the central axis. We write the equations in terms that are convenient here, and include the solution of the magnetic field inside the flux rope given by *Lundquist* [1951]. For simplicity gravitational forces are neglected.

$$\mathbf{j} \times \mathbf{B} - \nabla p = 0 \quad (\text{momentum equation}), \quad (1)$$

$$\nabla \cdot \mathbf{j} = 0 \quad (\text{charge conservation}), \quad (2)$$

$$\nabla \times \mathbf{B} = \mu_0 \mathbf{j} \quad (\text{Ampère's law}), \quad (3)$$

where \mathbf{j} is current density, \mathbf{B} is magnetic field, and p is pressure. If the pressure term of (1) is small relative to the magnetic field, then $\mathbf{j} \parallel \mathbf{B}$, and we can write

$$\mu_0 \mathbf{j} = \alpha \mathbf{B}, \quad (4)$$

where α is a scalar function of space. This is known as the force-free approximation, and its validity in the present case is discussed in section 11. Substituting (4) into (2) gives

$$0 = \nabla \cdot \alpha \mathbf{B}, \quad (5)$$

$$= \mathbf{B} \cdot \nabla \alpha + \alpha (\nabla \cdot \mathbf{B}). \quad (6)$$

[10] Since $\nabla \cdot \mathbf{B} = 0$ (no magnetic monopoles)

$$\mathbf{B} \cdot \nabla \alpha = 0. \quad (7)$$

[11] Equation (7) describes a function that has no variation in the direction of the magnetic field, that is to say α is constant along magnetic field lines. Substituting (4) into (3) gives

$$\nabla \times \mathbf{B} = \alpha \mathbf{B}, \quad (8)$$

which may be solved to find a consistent force-free magnetic field configuration.

[12] In the most simple model of a force-free flux rope, one that is straight, cylindrical, and with circular symmetry, α is a function of distance from the flux rope axis, and may be positive or negative. If α is constant everywhere inside the flux rope, equation (8) is linear. Beyond some defined edge of the flux rope there must exist the boundary condition $\mathbf{j} = 0$. The magnetic field in this current-free domain is a potential-field, where $\alpha = 0$.

[13] We utilize the solution of *Lundquist* [1951], in cylindrical coordinates, for the magnetic field inside a flux rope with constant α . The central axis of the flux rope is the z axis of the cylindrical coordinate system, and B_z is the magnetic field along the direction of the rope.

$$B_z = B_0 J_0(\alpha \rho), \quad (9)$$

$$B_\phi = B_0 J_1(\alpha \rho), \quad (10)$$

$$B_\rho = 0, \quad (11)$$

where J_0 , and J_1 , are the zeroth and first-order Bessel functions of the first kind. α is related to the radius of the flux rope, ρ_0 , by $\alpha = \pm j_{0,1}/\rho_0$. ($j_{0,1} = 2.40$ is the principal root of J_0 .) The scaling constant B_0 determines the magnitude of the magnetic field in the flux rope, which is related to the current flowing along the flux rope, I_z , and the radius, ρ_0 , as follows.

[14] Substituting (9) into (4) gives the current density along the axis of the flux rope

$$j_z = \frac{\alpha}{\mu_0} B_0 J_0(\alpha \rho). \quad (12)$$

The total current is found by integration over the circular cross section, using the property of Bessel functions: $xJ_0 = (xJ_1)'$

$$I_z = \frac{\alpha}{\mu_0} B_0 2\pi \int_{\rho=0}^{\rho_0} J_0(\alpha\rho) \rho d\rho, \quad (13)$$

$$= 2\pi \frac{\rho_0}{\mu_0} B_0 J_1(\alpha\rho_0). \quad (14)$$

Combining equations (10) and (14) defines the scaling constant and reveals an interesting property of the force-free flux rope

$$\frac{\mu_0 I_z}{2\pi\rho_0} = B_0 J_1(\alpha\rho_0) = B_\phi(\rho_0). \quad (15)$$

The right-hand side is the magnetic field at the boundary of the flux rope (since $B_z(\rho_0) = B_\rho(\rho_0) = 0$), while the left-hand side is recognizable as the magnetic field due to a long current carrying filament placed along the z axis.

[15] In fact, as long as the force-free approximation holds, the magnetic field everywhere outside the flux rope is that of a long straight filament, running along the flux rope axis, and carrying the same total current, I_z . This can be shown by decomposing the current into a series of concentric long solenoids, carrying current density j_ϕ , with a superimposed axial current, j_z . The magnetic field outside an infinite solenoid is zero. However, outside the flux rope the magnetic field due to the axial current is independent of its radial distribution according to Ampère's circuital law.

[16] Combining the above equations, we can describe the magnetic field of the flux rope in terms of its radius, ρ_0 , and current, I_z ,

$$B_z = \begin{cases} \frac{\mu_0 |I_z| J_0\left(\frac{\rho}{\rho_0} j_{0,1}\right)}{2\pi\rho_0 J_1(j_{0,1})}, & \rho < \rho_0 \\ 0, & \rho \geq \rho_0 \end{cases} \quad (16)$$

$$B_\phi = \begin{cases} \frac{\mu_0 I_z J_1\left(\frac{\rho}{\rho_0} j_{0,1}\right)}{2\pi\rho_0 J_1(j_{0,1})}, & \rho < \rho_0 \\ \frac{\mu_0 I_z}{2\pi\rho}, & \rho \geq \rho_0 \end{cases} \quad (17)$$

$$B_\rho = 0. \quad (18)$$

The core magnetic field is in the $+z$ direction. The current is parallel to the magnetic field when I_z is positive, and anti-parallel when I_z is negative. Inside the flux rope, at $\rho < \rho_0$, a current flows that is proportional to the magnetic field (α is constant). Whereas outside the flux rope, at $\rho > \rho_0$, there is zero current, and the model magnetic field is a potential field with closed field lines encircling the flux rope.

5. The Magnetic Field Surrounding a Flux Rope

[17] When a flux rope is located within a conducting plasma, the topology of the surrounding magnetic field

depends on the properties of the plasma, and the magnitude of the current in the flux rope. In the limiting case of zero conductivity in the surrounding plasma, and/or very large current in the flux rope, the magnetic field will be that of a current carrying filament: closed loops of magnetic field circling the flux rope, with magnitude falling linearly with distance from the rope's central axis. This limit may be applied to flux ropes in the solar corona.

[18] In the opposing limit, that of a flux rope carrying near-zero total current, surrounded by an infinitely conducting plasma, the flux rope can be treated as a solid obstacle, over which the frozen-in magnetic field of the surrounding plasma drapes. This is one of the approximations made by *Farrugia et al.* [1987] in modeling flux tubes associated with Flux Transfer Events at Earth's magnetopause. In their model, the flux tube is a cylinder, over which the frozen-in field of an inviscid, incompressible plasma is draped.

[19] In both limiting cases – the draped frozen-in field of *Farrugia et al.* [1987], or a potential field like that on the sun – outside the flux rope there is no magnetic field perturbation in the direction of the flux rope axis. Therefore, the orientation of the rope can be found by minimum variance analysis of the surrounding magnetic field.

[20] The flux ropes treated individually herein are very strong. Indeed, *Brain et al.* [2010] states that the flux rope seen on 9 March 2002 (example A) is to date the strongest encountered in situ. The magnetic field perturbations observed are of a similar magnitude to the strongest crustal magnetic fields measured at the altitude of MGS, which are able to exclude solar wind plasma to a degree sufficient to create cavities, commonly called minimagnetospheres.

[21] It is reasonable to suspect that such cavities might exist around strong flux ropes, leading to three regions. Inside the flux rope are helical, current-carrying magnetic field lines that are connected to the Martian crust. Immediately outside the flux rope the magnetic field resembles that of a current carrying filament: closed magnetic loops encircle the flux rope, their magnitude falling with radial distance until a boundary is met where the magnetic pressure is balanced by the external ram pressure. Around this the frozen-in field of the surrounding plasma will drape. By equating the magnetic pressure of the closed field lines encircling the flux rope with the external ram pressure, an estimate can be made for the magnetic field strength at the boundary separating the cavity from the surrounding plasma.

$$K\rho_i v^2 = \frac{|\mathbf{B}|^2}{(2\mu_0)}, \quad (19)$$

where v is the relative velocity between the external plasma and the flux rope, ρ_i is the ion mass density, and K is a pressure coefficient, which depends on the orientation of the frozen-in magnetic field, and the nature of the collisions between the ions and the boundary [*Schild*, 1969]. Typical values are $K = 0.8$, $v = 10 \text{ km s}^{-1}$, and $\rho_i = 10^{-18} \text{ kg m}^{-3}$, giving a magnetic field strength of $|\mathbf{B}| = 14 \text{ nT}$ at the boundary. A more precise value of 20 nT is obtained by integrating the differential flux densities of ions, including high energy populations of solar wind protons and alpha

particles, given by Nilsson *et al.* [2012] for the sub-IMB (induced magnetosphere boundary) terminator region. This is smaller than the magnetic field magnitudes observed around the flux ropes in Figure 2, suggesting that cylindrical

minimagnetospheres are likely to exist around the larger flux ropes.

6. Fitting the Model Flux Rope

[22] Figure 1 shows the model magnetic field of a z -aligned flux rope, with unity radius ($\rho_0 = 1$ m), and unity total current ($I_z = 1$ A). In Figure 1a the current and magnetic field are parallel, whereas in Figure 1c they are anti-parallel. Hodograms of the model magnetic field are shown for each case in Figures 1b and 1d. Three straight trajectories are shown, each with a different impact parameter. Trajectory (i) passes at a minimum distance of $1.1 \rho_0$, i.e. never penetrating the flux rope, (ii) at $0.8 \rho_0$, and (iii) passes directly through the center of the structure. Outside the flux rope the lines are colored red, inside they are blue. Each of the trajectories produces a distinct hodogram trace, which are described below.

6.1. Type i

[23] Passing by the flux rope without entering it produces a circular hodogram trace. From this, estimates can be made for the following parameters. The orientation of the flux rope may be found by minimum variance analysis of the magnetic field outside the flux rope, since the central axis of a flux rope is perpendicular to the plane of rotation of the magnetic field vector. The magnitude and direction of the total current in the flux rope simply scales the measured magnetic field.

[24] The location of the flux rope is reduced to two degrees of freedom because the model flux rope follows a straight line. The first location parameter is given by the position along the spacecraft's orbit of maximum $|\mathbf{B}|$. The second location parameter is found by combining knowledge of: the orientation of the flux rope; on which side of the spacecraft the flux rope is passed, indicated by the rotational direction of the hodogram trace; and the impact parameter, i.e. the distance of closest approach between the spacecraft and the center of the flux rope. The impact parameter affects the duration of a flux rope signature in the data; a nearby weak flux rope is traversed more quickly than a strong distant one.

6.2. Type ii

[25] The second type is arguably the most distinctive. The point at which the flux rope boundary is crossed corresponds to an out-of-plane bend in the circular trace, which may alternatively be described as a rotation of the minimum variance plane. In addition to the parameters that may be estimated from the magnetic field outside the flux rope, which are the same as for type (i) above, it is also possible to infer the radius of the flux rope, ρ_0 , and the direction of the core magnetic field: parallel, or anti-parallel to the current.

[26] The radius of the flux rope is found by combining the impact parameter, and the points at which the spacecraft enters and exits the flux rope, according to the out-of-plane bend in the hodogram. The core magnetic field direction is indicated by the direction of the out-of-plane bend.

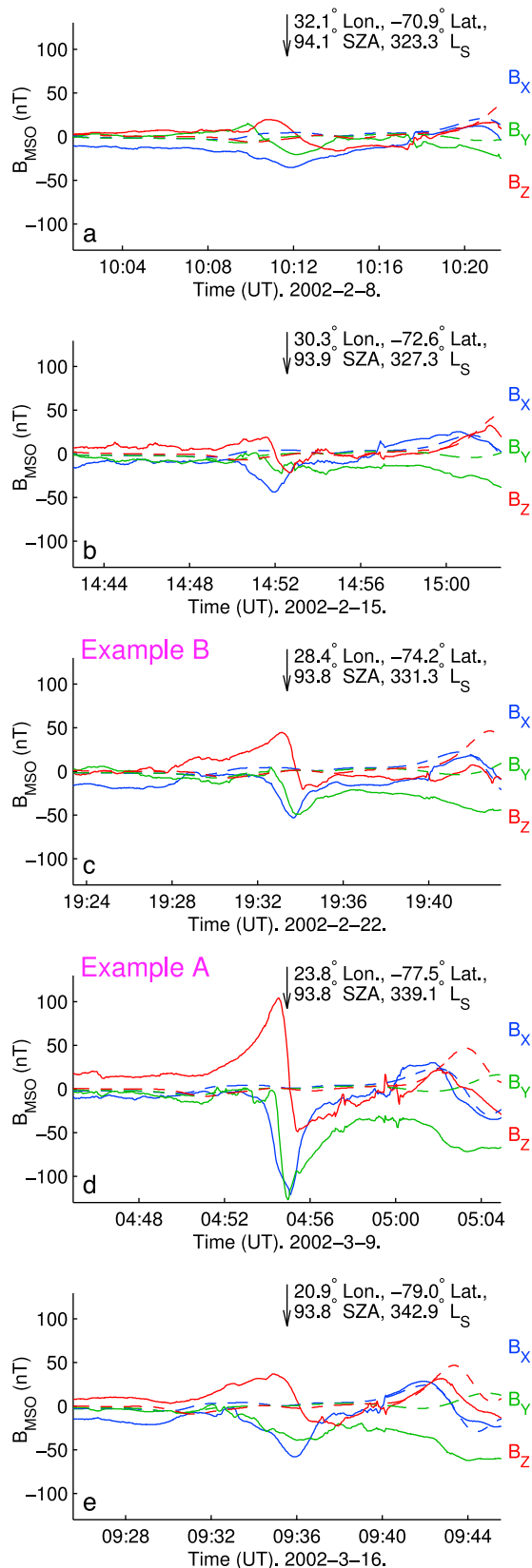


Figure 1. Magnetic field measurements from the same MSO location. The panels are separated by complete cycles of 88 orbits. The center of each panel, marked with an arrow, is the closest location, in MSO coordinates, to that of maximum $|\mathbf{B}|$ during example A.

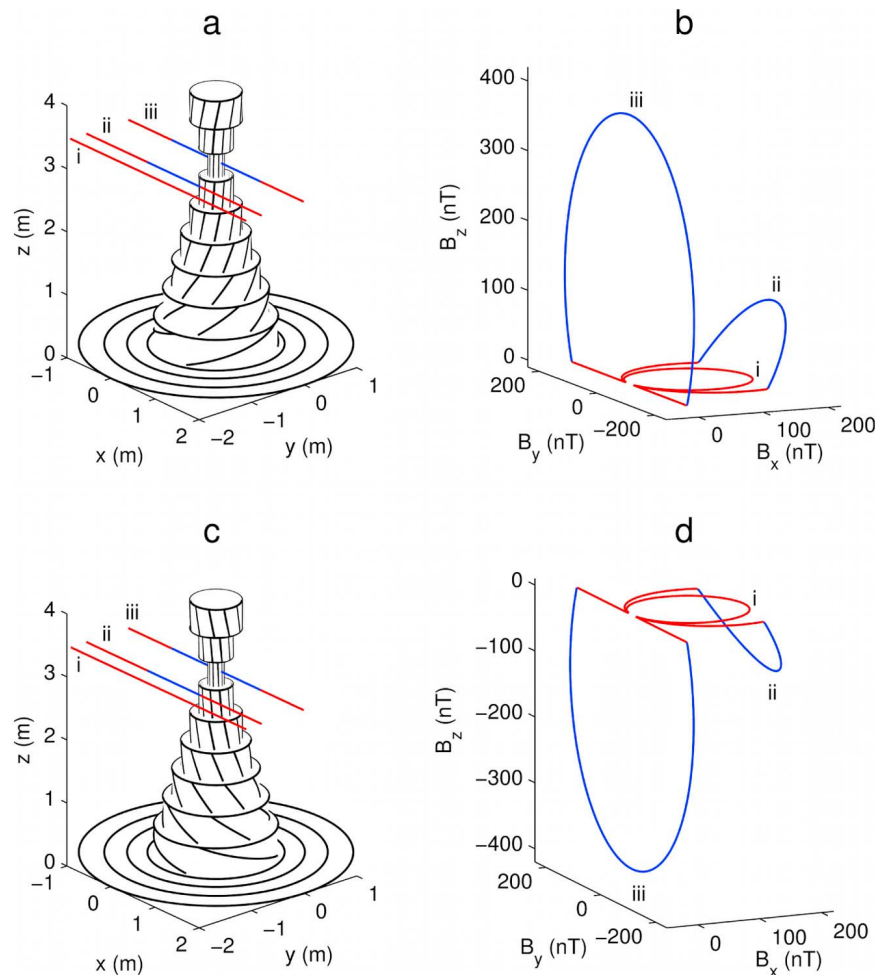


Figure 2. The model force-free flux rope. Cross sections illustrate the magnetic field in and around the flux rope when the core current is in the $+z$ direction and the magnetic field is (a) parallel and (c) anti-parallel to the current. In each case the total current is 1 A, and the flux rope radius is 1 m. (b, d) The corresponding magnetic hodograms for three straight trajectories of varying impact parameter: (i) $1.1 \rho_0$; (ii) $0.8 \rho_0$; and (iii) 0.

6.3. Type iii

[27] Passing directly through the center of the flux rope produces a circular trace with a flattened section. In some cases this might be hard to distinguish from trajectory (i), leading to a 90° error in the inferred orientation of the flux rope axis.

7. Results

[28] In this section we fit the model to three flux ropes observed at the southern terminator of Mars. The first two, labeled A and B, belong to the group of recurring flux ropes shown in Figure 2. In example C, the planet is rotated so that a different longitude is beneath the sub-solar point.

[29] To fit the model to each observation, the minimum variance plane is calculated for data outside the flux rope. The normal to this plane is then taken to be the flux rope axis. The position of the model flux rope is shifted, and the radius and current are simultaneously adjusted, until the model fits the data. This can be achieved with relatively little ambiguity, since each variable controls a different aspect of

the result. Each of the flux ropes were found to be below the 400 km mapping altitude of MGS, and close to horizontal.

[30] The values of the parameters used in the fitted model for each of the flux rope examples are given in Table 1. The corresponding error values are the ranges over which the goodness-of-fit, taken to be the mean of the squared residuals, remains within a factor of two of the minimum value. This gives an indication of the accuracy of each value. As each parameter is varied to find its acceptable range, the other parameters are simultaneously varied to preserve the best possible fit.

7.1. Example A

[31] Our first example is the flux rope signature present in Figure 2d. This is the same event discussed by *Brain et al.* [2010]. Figures 3a–3c show magnetic field hodograms of the flux rope signature. Principal variance analysis of the magnetic field outside, but close to, the flux rope is used to define the coordinate system. The minimum variance direction, n , is aligned with the flux rope axis. The corresponding maximum variance direction is l , and m completes the

Table 1. Values Used in the Fitted Flux Rope Model Shown in Figures 3d–3f, Figures 4d–4f, and Figures 5d–5f^a

Example	Encounter Time (UT)	Closest Distance (km)	Radius (km)	B-Field Direction	Current Direction	Current (kA)
A	2002-03-09 04:54:50	108 ± 25	140 ± 19	Dawn/Sun	Dusk/tail	91.2 ± 8.5
B	2002-02-22 19:33:36	129 ± 18	<129	Unknown	Dusk/tail	45.4 ± 3.5
C	2003-08-26 18:18:11	77.2 ± 40	82.6 ± 33	Dawn/Sun	Dusk/tail	19.3 ± 6.1

^aA range is given for each variable, over which the goodness of fit (mean of squared residuals) can be kept within a factor of two. The third column is the closest distance from the MGS spacecraft to the center of each flux rope. The exact orientations used in the flux rope model are calculated by minimum variance analysis and are shown in Figures 3g, 4g, and 5g.

orthogonal set. The out-of-plane bend in the trace indicates the entry and exit points as the spacecraft passes through the flux rope. Inside the flux rope the line is colored blue, outside it is red.

[32] Figures 3d–3f are the individual components of the magnetic field in MSO coordinates. The colored line is the data, with colors matching the above panels, and the black lines are the fitted model results. The boundary of the model flux rope is indicated by vertical lines. The model fits the data well, with the exception of the Y component outside the flux rope, where there is a uniform offset in the observed magnetic field. No changes in the model parameters could possibly account for this constant offset, which could be due to, for example, currents in the dynamo region of the ionosphere. Such currents would produce magnetic fields that add linearly to the near potential field surrounding the flux rope, but would have no B_z component, since at this location the Z direction is perpendicular to the ionosphere. In B_z the model follows the measured perturbation very closely for ~1000 km into the night side.

[33] A diagram showing the fitted model flux rope (including its width, position, and orientation), together with the path of MGS, is presented in Figure 3g. The model flux rope is in green, and the path of MGS corresponding to the period of data in Figures 3d–3f is in black. The view is from the $-Z$ direction, looking toward the south polar region of the planet, with the sun at the top. The planet is colored according to the radial crustal magnetic field strength from the *Cain et al.* [2003] model. Regions of strong crustal field are located on the day side, upstream of the flux rope.

[34] Panel h shows the electron flux from the lowest energy bin of the electron reflectometer, which responds to electrons with energies from 10 eV to 13 eV. There is a reduction in electron flux at either side of the flux rope, with a greater drop downstream of the rope. The boundary of the model rope is indicated by the vertical lines. A partial void beyond the edge of the flux rope could be evidence of a cylindrical mini-magnetosphere similar to those formed by the crustal magnetic fields, the result of a stand-off between magnetic pressure generated by the flux rope current, and the dynamic pressure of the surrounding plasma.

[35] Data from the electron reflectometer are known to be affected by spacecraft charging, and secondary electrons, caused by photons and energetic particles impacting the spacecraft. These errors occur primarily in the low energy channels (<100 eV), and can strongly influence measured pitch angle distributions [*Uhsen et al.*, 2011]. The event took place during a relatively quiet period, reducing the likelihood of energetic particle influence. The orientation of the spacecraft just before and after the encounter with the flux rope could have caused self-shadowing of a particular part of the spacecraft or instrument, resulting in erroneous measurements.

However, this seems unlikely in view of similar drops in the electron flux observed before and after the encounter with flux rope example C (Figure 5h), during a different time of the Martian year, and with a spacecraft orbit that is shifted with respect to the sun.

7.2. Example B

[36] The second flux rope example occurred two 88-orbit cycles before example A. In Figure 2 the magnetic signature looks very similar to that of example A, but in the hodograms (Figures 4a–4c) the trace does not appear to contain the same characteristic out-of-plane bend. The region of data that shows a clean flux rope signature, free from extraneous fields, creates a partial circle in the hodogram. This trace could belong to a grazing trajectory, similar to Figure 1a, or to a path directly through the center of the flux rope (Figure 1c). However, two factors point to this being one of the former. Firstly, if the trajectory is assumed to be grazing, the inferred flux rope orientation is similar to that of its twin, example A, but in the case of a direct hit, the axis of the flux rope would be rotated by 90°. Secondly, as the spacecraft passes the flux rope, it coincides with a small reduction in the electron flux, Figure 4h. The reduction does not show the double dip observed in the other examples as the spacecraft twice passes the boundary of the flux rope. A single, small reduction is plausible for a grazing pass of a cavity surrounding the flux rope.

7.3. Example C

[37] The third event, presented in Figure 5, is a clear example of a spacecraft trajectory that enters the boundary of the flux rope. The out-of-plane bend direction of Figure 5b indicates the current is anti-parallel to the magnetic field. Figures 5d–5f show that the model does not match the data well outside the flux rope boundary. This is reflected in the large ranges for the parameter values given in Table 1. Far from the flux rope the measured magnetic field deviates further from zero, an impossible case for a single straight flux rope model. A possible explanation for the observed magnetic field is that it is the combined field from multiple flux ropes. In Figure 5c the departure from a circular hodogram trace near the end (E), is a candidate for a second flux rope crossing. If this is another flux rope, it appears to be perpendicular to the first.

[38] Figure 5h shows a clear reduction in the electron flux surrounding the flux rope. Downstream of the rope, i.e., at earlier times, a wave-like structure appears in the electron flux. These structures, observed in the wakes of the stationary flux rope obstacles, will be investigated in a future study.

8. Formation of a Flux Rope

[39] In this section we propose a mechanism for the formation of a flux rope from stretched crustal magnetic

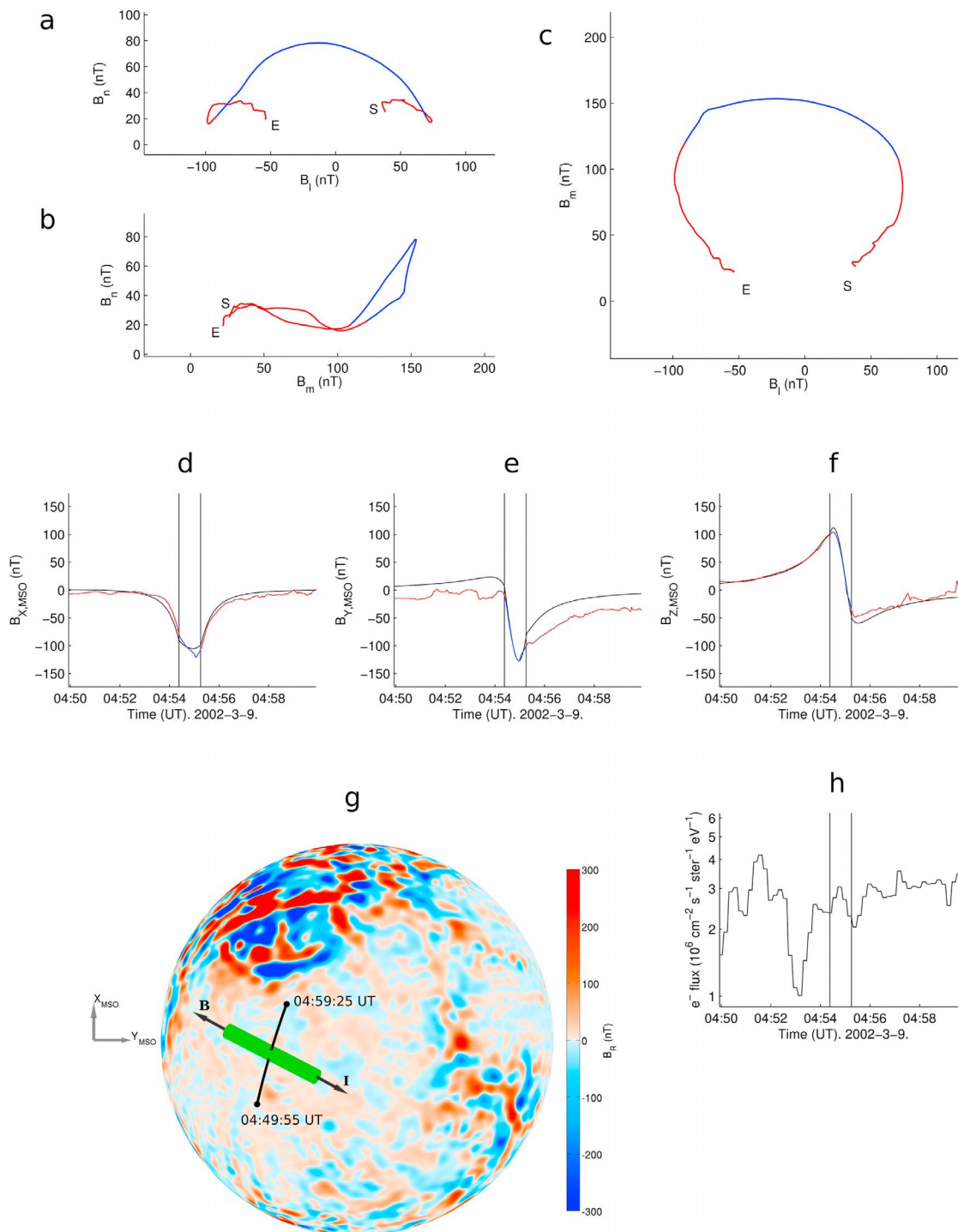


Figure 3. Example A, on 9 March 2002. (a–c) Hodograms of the magnetic field in flux rope orientated coordinates (n is the flux rope axis). The letters S and E mark the start and end points of the trace. The line is colored blue inside the flux rope and red outside. (d–f) Comparisons of each MSO magnetic field component with the fitted model values. The blue and red colors again correspond to inside and outside the flux rope, respectively. The vertical lines indicate the boundary of the model flux rope. (g) An illustration of Mars from the $-Z_{MSO}$ direction. The black line represents the path of MGS during the time period covered by Figures 3d–3f. The fitted model flux rope is shown in green. The planet is colored to show the radial magnetic field strength from the *Cain et al.* [2003] crustal magnetic field model. (h) The electron flux measured by the 10 eV to 13 eV channel of the electron reflectometer.

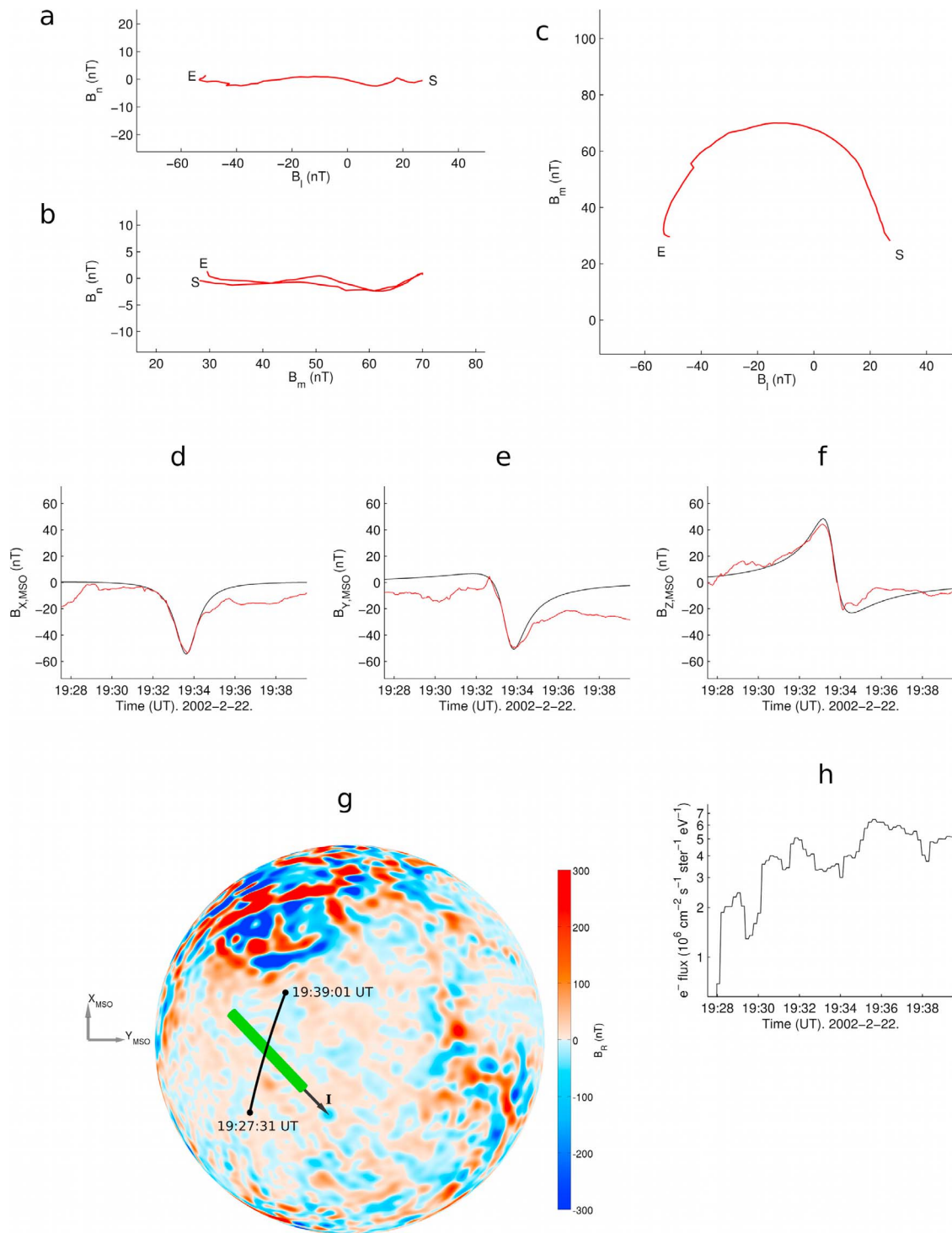


Figure 4. Example B. As in Figure 3, except for the second flux rope example, on 22 February 2002.

fields. As crustal magnetic field lines are stretched further from their source, it is expected that they will reach a point where reconnection occurs, and a plasmoid may break away [Brain *et al.*, 2010]. In order to see how a similar process could form flux ropes, which remain attached to the crust, it is necessary to consider the problem in three dimensions.

[40] Figure 6 illustrates the formation of a flux rope in four stages:

[41] 1. The field is stretched downstream (toward the reader), from an elongated crustal magnetic dipole. In general, the flow direction of the plasma will not be exactly aligned with the magnetic dipole axis, resulting in field lines that overlay neighboring field lines. Had the dipole been aligned exactly with the flow, each outgoing field line would return directly above, or below itself.

[42] 2. The field is stretched to the point at which reconnection occurs. Magnetic field lines reconnect with

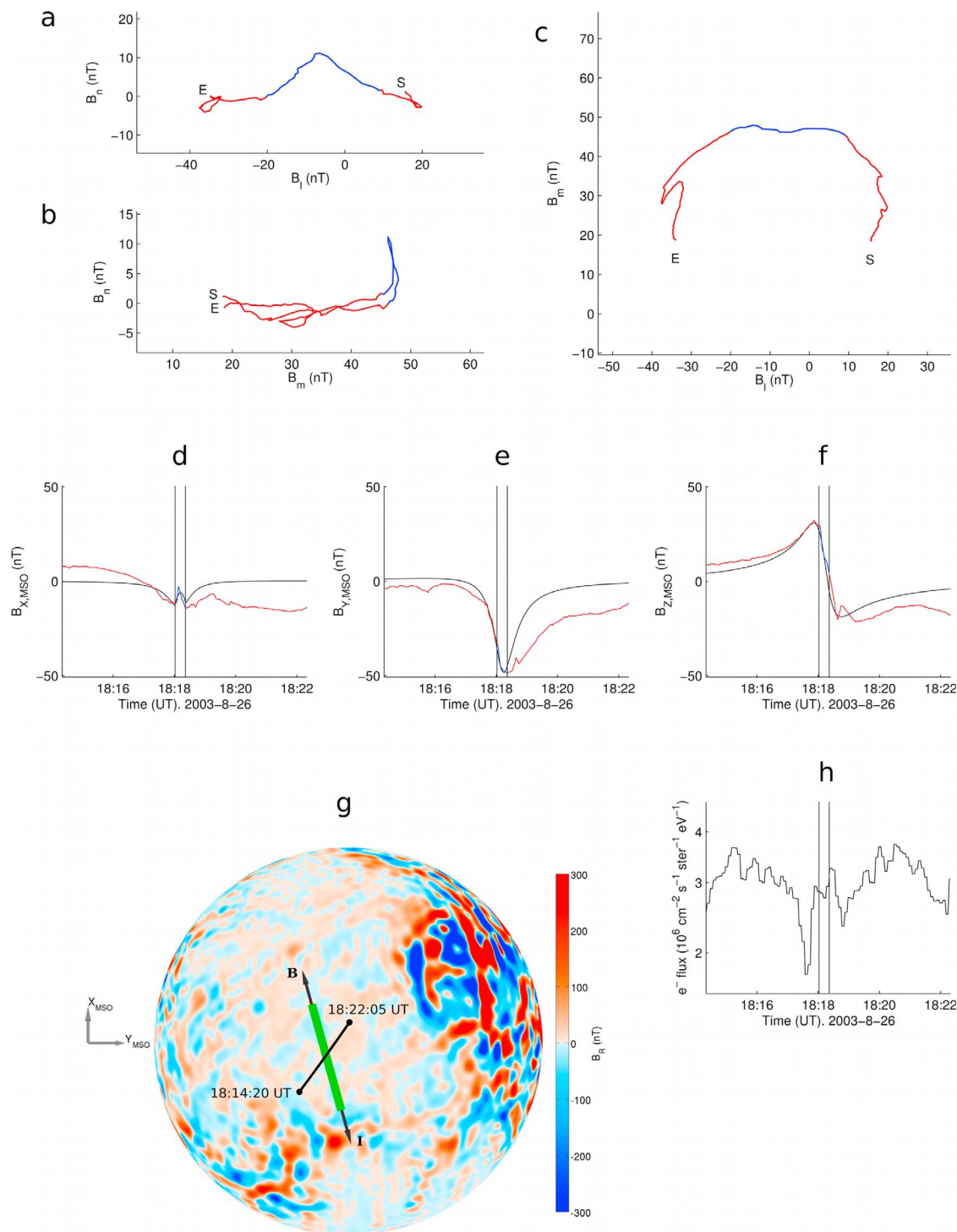


Figure 5. Example C. As in Figure 3, except for the third flux rope example, on 26 August 2003.

neighbors, forming the beginning of a helical flux rope. The newly formed section of flux rope is less strongly anchored to the crust, while the cylindrical cross section presents a larger area for the ram pressure of the plasma to act upon.

[43] 3. The additional dynamic force, and weaker anchoring to the crust, quickens the reconnection process as it propagates along the length of the structure like a zipper.

[44] 4. A complete flux rope is formed. It is still attached to the crust, and the structure is relatively stable, requiring a

large reconfiguration of the magnetic field in order to break away from the crust.

[45] According to this mechanism, the direction of the current inside the flux rope will depend on whether the north or south pole of the crustal magnetic field is further downstream. Similarly, the direction of the core magnetic field in the flux rope, either parallel or anti-parallel to the current, will depend on the relative position of the crustal magnetic poles in the direction perpendicular to the plasma velocity.

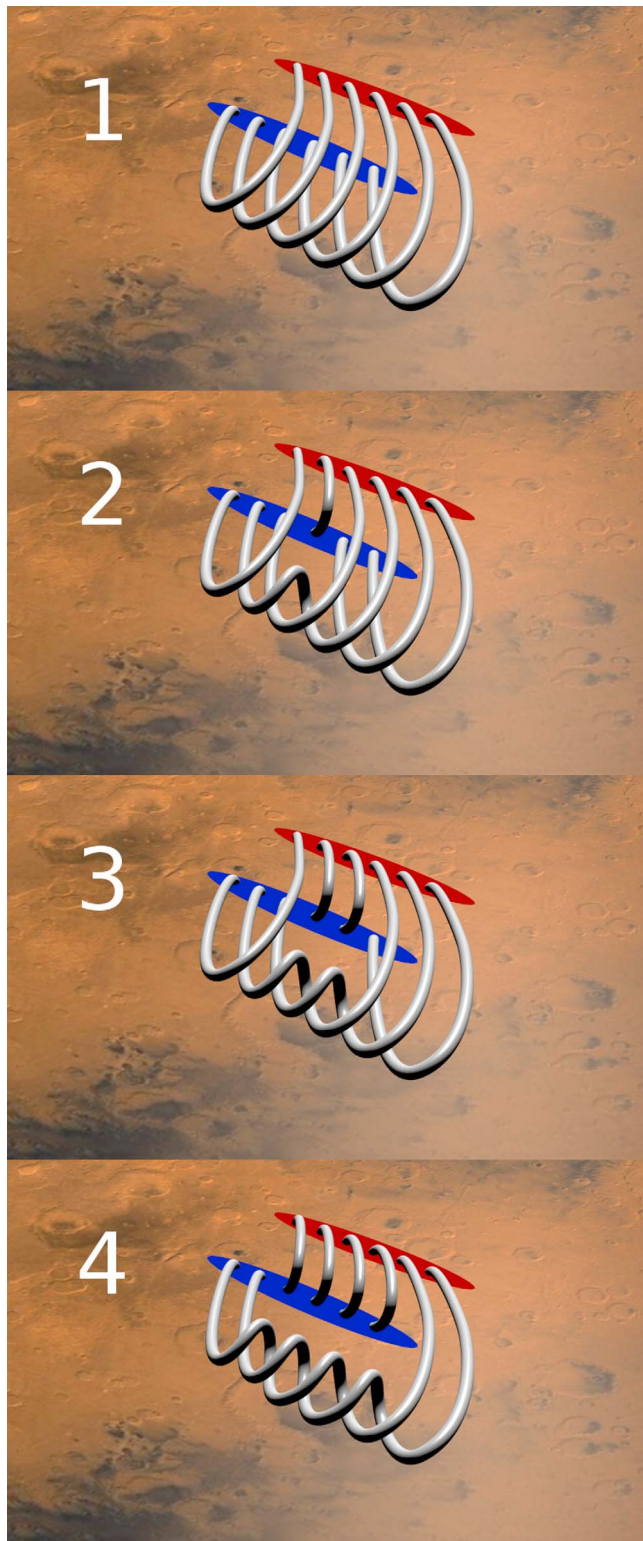


Figure 6. A proposed mechanism for the formation of flux ropes by the stretching of crustal magnetic fields.

Therefore, by rotating the crustal magnetic field through 360° , each of the four possible configurations of current direction and field direction inside the flux rope can be produced. If the individual crustal magnetic fields associated with observed flux ropes could be identified, a comparison

of their orientation at the time of flux rope formation, with the properties of the flux ropes, would provide some verification of the above mechanism. Additionally, it might be possible to employ multifluid simulations [e.g., *Harnett and Winglee, 2007*] to investigate the mechanism.

9. Spatial Distribution of Flux Ropes

[46] So far we have mostly considered a particular set of recurring flux rope signatures, each found at the same location near the southern terminator. In order to see whether there is something special about this location it is useful to search the MGS mapping phase data set for more events. In the simplest terms, the magnetic signature of a flux rope is a deviation from the crustal magnetic field on a timescale of around 1–2 min. By applying a sliding median function to the data, with a similar window size, it is possible to find many such magnetic anomalies. During solar storms, large deviations from the crustal magnetic field exist over much longer timescales. In order to avoid the detection of these, the function is divided by a sliding median with a longer window. Forty-five s is chosen for the short window, and 20 min for the long window. A detection threshold of 1.35 is used, which is found to give a reasonable number of events (7332 at southern co-latitudes). Increasing the threshold to 1.5 reduces the number of detected events by a factor of two, without noticeably affecting their spatial distribution. An event is recorded when

$$\frac{\mathbf{M}_{45}(|\mathbf{B}| - |\mathbf{B}_{\text{Cain}}|)}{\mathbf{M}_{1200}(|\mathbf{B}|)} \geq 1.35, \quad (20)$$

where \mathbf{M}_n is the sliding median function with a window size of n s, and \mathbf{B}_{Cain} is the crustal magnetic field taken from the *Cain et al.* [2003] model. If multiple detections are made within 1 min of data, all but one are discarded, and a single event is recorded. While this method is intended to detect flux rope signatures, other anomalous magnetic features, such as current sheets, may also be included if they have sufficient magnitude, and are of a similar duration. The parameters used in the detection were chosen by manually looking at random samples of the detected events and judging their quality. The majority of detected events contain rotations in the magnetic field vector similar to flux rope signatures, although some were current sheets, or flux ropes embedded in current sheets, and others were too complex to allow distinct flux ropes to be identified. Due to the simple automated method of detection, we must stress that these results should be treated as preliminary, and further work needs to be done to accurately identify flux ropes in the large data set. However, the events detected near the terminator did not appear to be any less valid than those found elsewhere. A more manual approach to flux rope identification has been applied to smaller subsets of MGS data by *Vignes et al.* [2004] and *Briggs et al.* [2011].

[47] In Figure 7a, the frequency of events are shown as a function of solar zenith angle, with the data restricted to southern co-latitudes only ($Z_{\text{MSO}} < 0$). There is a clear peak at solar zenith angles between 90° and 100° . Applying cubic-spline interpolation gives an estimate of 93.7° for the modal value, closely matching the solar zenith angles of the observed flux ropes in Figure 2.

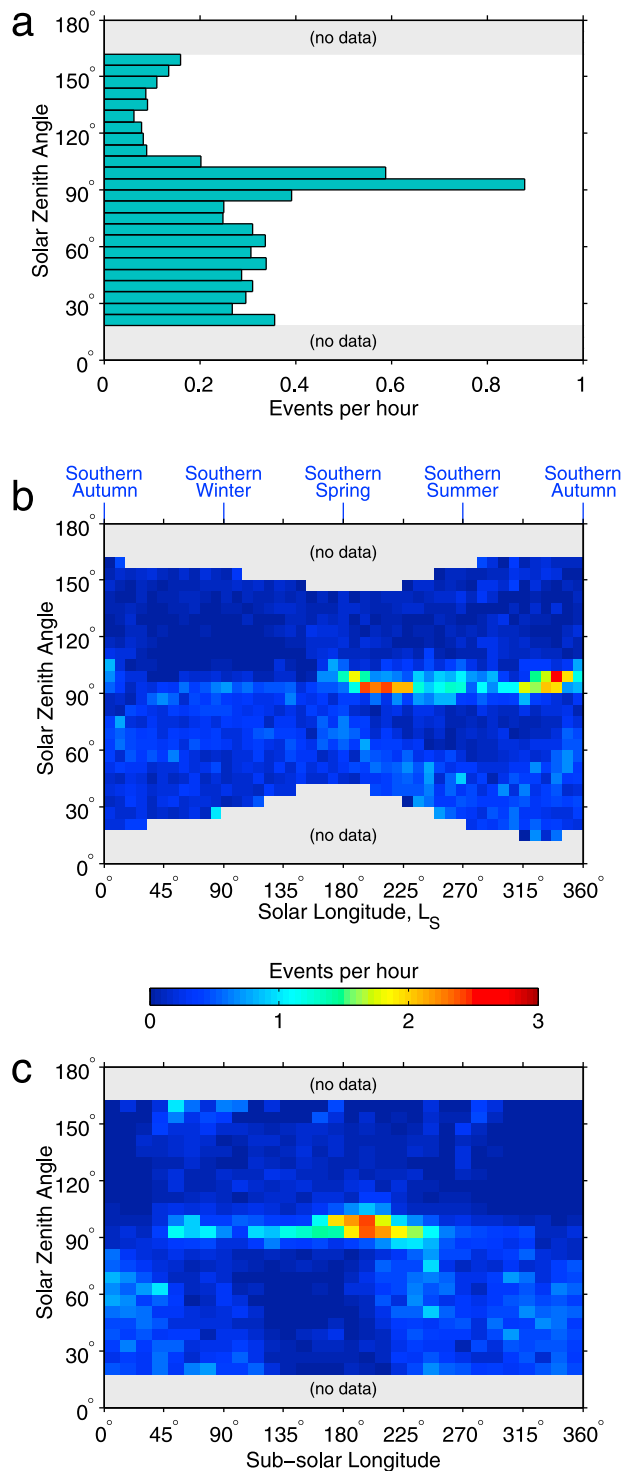


Figure 7. Distributions of minute-scale magnetic anomalies, including flux ropes, as a function of (a) solar zenith angle; (b) solar longitude and solar zenith angle; and (c) sub-solar longitude and solar zenith angle.

[48] In Figure 7b, the events are separated according to the Martian season. Most of those near the terminator are observed at solar longitudes between 180° and 360°, i.e. between southern hemisphere spring and autumn. During this

time of year the strong crustal magnetic fields in the southern hemisphere are shifted toward the sub-solar point, allowing attached flux ropes to cross the terminator region. Whereas, in southern hemisphere winter, any crustal magnetic fields at latitudes south of -65° are on the night-side, and therefore downstream of the terminator, at all times of day.

[49] Figure 7c shows the frequency of the southern co-latitude events as a function of sub-solar longitude (planetary rotation), and solar zenith angle. A strong peak near 180° sub-solar longitude indicates that the events are more likely when the strong crustal magnetic fields, which are found near 180° longitude, are on the day-side, upstream of the terminator. Interestingly, over a large range of sub-solar longitudes there is no change in the preference for solar zenith angles near the terminator. It appears that events are preferentially found at the terminator no matter where on the day side the crustal magnetic fields are located.

[50] An investigation of 104 Martian flux ropes by *Vignes et al.* [2004] reported similar results: most of the ropes occurred near the terminator plane, with a mean solar zenith angle of 80°. However, *Vignes et al.*'s results were limited to the northern hemisphere of Mars. The *Briggs et al.* [2011] statistical study of 360 magnetic structures covered both hemispheres. Their results do not show the same strong preference for the terminator, although the densities of flux ropes at solar zenith angles greater than 100° are clearly less than those at smaller solar zenith angles.

[51] The recurring flux rope signatures in Figure 2 are at solar zenith angles of around 94°, and solar longitudes between 323° and 343°, placing them in the cluster of events at the right-hand side of Figure 7b, where 2–3 events are detected for each hour of data. The sub-solar longitude in each case is around 199°, matching the cluster of events near the center of Figure 7c.

[52] The flux rope we have labeled example C, observed on 26 August 2003, has a solar zenith angle of 94.4°, a solar longitude of 249°, and a sub-solar longitude of 102°. Figures 7b and 7c suggest that flux ropes with these values are less common than our other flux rope examples, but still lie within a band of enhanced frequency near the terminator.

10. Why at the Terminator?

[53] In the previous section the results indicate that flux ropes (and other similar magnetic anomalies) are observed preferentially at the terminator. This is true over a range of solar longitudes, and sub-solar longitudes. It is unclear if there is a preference for flux rope loops to stop at the terminator, or to stretch further downstream, passing the terminator plane at an altitude close to that of the 400 km mapping orbit of MGS. The low altitudes of the flux ropes in Figure 2, and those studied by *Vignes et al.* [2004] (246 ± 156 km), suggest that they should be observed at altitudes below MGS for solar zenith angles between approximately 92° and 102°, and above MGS between 102° and 112°. We find that, in agreement with *Vignes et al.* [2004] and *Briggs et al.* [2011], considerably fewer flux rope observations are made between 102° and 112° than between 92° and 102°, suggesting that many of the flux ropes do not extend far past the terminator. Furthermore, in the case of a flux rope that extends much further down stream, the orientation of the rope at the terminator should be toward/away from the sun. This is not the

case for the near identical recurring flux ropes investigated in this paper. Therefore, we consider the possibility that they preferentially stop at, and run along, the terminator. There are (at least) two possible reasons why flux rope loops, stretched downstream by the plasma flow, may reach a state of static equilibrium at the terminator.

[54] The sharp conductivity gradient at the terminator may cause a reduction in the current as the flux rope transitions into the night side. This would cause a reduction in the stand off distance between the magnetic field encircling the flux rope and the surrounding plasma, effectively reducing the cross section of the flux rope, and therefore the force pushing it toward the night side.

[55] Alternatively, the reduced conductivity in the night side could cause the process described in section 8 to partially reverse. Fewer magnetic field lines would be inside the flux rope, and more would connect the structure back to the crust. The further the flux rope moves into the night side, the lower the conductivity, the more the flux rope “unwraps”, and the stronger it is pulled back toward the day side by the additional connected field lines.

[56] It could be that in many cases a flux rope will not reach a state of static equilibrium at the terminator, but our observations are biased toward those events that remain long enough for the spacecraft to pass by and measure them.

11. Validity of the Model

11.1. Magnetic Field Surrounding a Curved Flux Rope

[57] In the most basic model, where no current flows outside a straight flux rope, the external magnetic field is a potential field with a minimum variance direction that is aligned with the axis of the rope. However, the stationary flux ropes at Mars are bent, stretched, or otherwise dragged downstream by the local plasma motion. Recently, *Petrie* [2007] presented analytic solutions for the potential magnetic field outside curved flux ropes. In such cases the external magnetic field parallel to the flux rope can be non-zero, breaking the assumption that the minimum variance direction will be aligned with the flux rope axis. However, it is unlikely that curvature of a flux rope would cause any significant error in the inferred axis when the minimum variance direction is obtained close to the boundary of the flux rope, as it is here.

11.2. The Force-Free Approximation With Constant α

[58] Our model consists of a force-free flux rope with a step-function $\alpha(\rho)$ that is constant inside the boundary of the flux rope, and zero outside. Physically, this means that a current flows inside the flux rope, but no current flows outside.

[59] A constant α is not necessary throughout the entire force-free flux rope, only along each individual field line. Entirely constant α corresponds to the minimum magnetic energy in a closed system with zero resistivity [*Woltjer*, 1958; *Taylor*, 1974], and is therefore the preferred configuration for such a case. However, the observed Martian flux ropes are neither closed systems, being attached to crustal magnetic fields through the conductive ionosphere, while the surrounding plasma stretches them downstream; nor do they have zero resistivity.

[60] In flux rope example C, the magnetic field hodogram, Figure 5b, shows an out-of-plane bend greater than 90° , as the spacecraft passes through the flux rope. This angle is greater than predicted by the model for a similar impact parameter (Figure 1b). A breakdown of the force-free, or constant α assumptions may account for the larger observed angle. A larger angle in the out-of-plane bend implies that the magnetic field at the core of the flux rope is weaker than predicted by the constant α model, or alternatively the field at the edge is stronger than predicted. Intuitively it can be visualized that the straight current in the core of the flux rope contributes to the toroidal magnetic field at the edge, while the toroidal current at the edge contributes to the straight magnetic field at the center. Since the current near the edge of the flux rope must travel a longer path than the current in the center, a uniform finite resistivity will reduce the current at the edge of the rope relative to the center. In a plasma of finite uniform conductivity it may be expected that the magnetic field at the core of the flux rope will be relatively reduced, matching the observation.

[61] The empirical models of *Elphic and Russell* [1983], and *Russell* [1990] are based on a number of free parameters that are fitted to the magnetic signatures of Venusian flux ropes. Out-of-plane bends are observed in all but one of the example hodogram traces presented by *Russell* [1990]. Instead of a sharp kink, the bends usually appear more gradual, and are described as a warping of the minimum variance direction. In contrast, the hodograms of Martian flux ropes often show a well defined boundary (see, e.g., Figures 3b and 5b). A possible explanation for this could be that the clear boundary around large Martian flux ropes separating the inside, where the magnetic field lines are connected to the crust and carry a current, from the outside, where the field may form closed loops within a mini-magnetosphere cavity, does not apply to the Venusian flux ropes, which are not attached to any crustal magnetic fields.

12. Conclusion

[62] Large flux rope signatures at the southern terminator of Mars are repeatedly observed at the same location, indicating that they are not moving with the local plasma velocity of $5\text{--}15\text{ km s}^{-1}$ but are stationary. In order to produce near-identical signatures in each successive 88-orbit cycle, the flux ropes must be attached to the planet. Since the events are located at a constant solar zenith angle, and not a constant planetary latitude, the possibility that they are misidentified crustal magnetic field signatures can be ruled out.

[63] A model force-free flux rope is fitted to three of the magnetic signatures, two of which belong to the same repeating set, and several parameters of the flux ropes are inferred. The largest flux rope is estimated to have a radius of 140 km, and carry a current of 95 kA.

[64] We suggest a mechanism by which stable flux ropes can be formed by the stretching of crustal magnetic fields. Properties of the flux ropes produced by this mechanism will depend on the orientation of the crustal magnetic field at the time of the flux rope formation. This provides a means to test the proposed mechanism—if the crustal magnetic field sources can be identified for a sufficient number of flux ropes.

[65] **Acknowledgments.** The MGS dataset is obtained from NASA's Planetary Data System archive (<http://pds.nasa.gov/>). We are grateful to everyone involved in the production and provision of these data. MJB and JAW are both supported by STFC grant STG002320/1.

[66] Masaki Fujimoto thanks the reviewers for their assistance in evaluating this paper.

References

- Brain, D. A., A. H. Baker, J. Briggs, J. P. Eastwood, J. S. Halekas, and T.-D. Phan (2010), Episodic detachment of Martian crustal fields leading to bulk atmospheric plasma escape, *Geophys. Res. Lett.*, *37*, L14108, doi:10.1029/2010GL043916.
- Briggs, J. A., D. A. Brain, M. L. Cartwright, J. P. Eastwood, and J. S. Halekas (2011), A statistical study of flux ropes in the Martian magnetosphere, *Planet Space Sci.*, *59*, 1498–1505.
- Cain, J. C., B. B. Ferguson, and D. Mozzoni (2003), An $n = 90$ internal potential function of the Martian crustal magnetic field, *J. Geophys. Res.*, *108*(E2), 5008, doi:10.1029/2000JE001487.
- Elphic, R. C., and C. T. Russell (1983), Magnetic flux ropes in the Venus ionosphere: Observations and models, *J. Geophys. Res.*, *88*(A1), 58–72, doi:10.1029/JA088iA01p00058.
- Elphic, R. C., and D. J. Southwood (1987), Simultaneous measurements of the magnetopause and flux transfer events at widely separated sites by AMPTE UKS and ISEE 1 and 2, *J. Geophys. Res.*, *92*(A12), 13,666–13,672, doi:10.1029/JA092iA12p13666.
- Farrugia, C. J., R. C. Elphic, D. J. Southwood, and S. W. H. Cowley (1987), Field and flow perturbations outside the reconnected field region in flux transfer events: Theory, *Planet Space Sci.*, *35*(2), 227–240.
- Gold, T., and F. Hoyle (1960), On the origin of solar flares, *Mon. Not. R. Astron. Soc.*, *120*(2), 89–105.
- Harrett, E. M., and R. M. Winglee (2007), High-resolution multifluid simulations of the plasma environment near the Martian magnetic anomalies, *J. Geophys. Res.*, *112*, A05207, doi:10.1029/2006JA012001.
- Hasegawa, H., B. U. Ö. Sonnerup, C. J. Owen, B. Klecker, G. Paschmann, A. Balogh, and H. Rème (2006), The structure of flux transfer events recovered from Cluster data, *Ann Geophys.*, *24*, 603–618.
- Lundquist, S. (1951), On the stability of magneto-hydrostatic fields, *Phys. Rev.*, *83*, 307–311, doi:10.1103/PhysRev.83.307.
- Morgan, D. D., D. A. Gurnett, F. Akalin, D. A. Brain, J. S. Leisner, F. Duru, R. A. Frahm, and J. D. Winningham (2011), Dual-spacecraft observation of large-scale magnetic flux ropes in the Martian ionosphere, *J. Geophys. Res.*, *116*, A02319, doi:10.1029/2010JA016134.
- Nilsson, H., G. Stenberg, Y. Futaana, M. Holmström, S. Barabash, R. Lundin, N. J. T. Edberg, and A. Fedorov (2012), Ion distributions in the vicinity of Mars: Signatures of heating and acceleration processes, *Earth Planets Space*, *64*, 135–148.
- Petrie, G. J. D. (2007), Potential magnetic field around a helical flux rope current structure in the solar corona, *Astrophys. J.*, *661*, 551–557.
- Russell, C. T. (1990), Magnetic flux ropes in the ionosphere of Venus, in *Physics of Magnetic Flux Ropes*, *Geophys. Monogr. Ser.*, vol. 58, edited by C. T. Russell, E. R. Priest, and L. C. Lee, pp. 413–423, AGU, Washington, D. C., doi:10.1029/GM058p0413.
- Schild, M. A. (1969), Pressure balance between solar wind and magnetosphere, *J. Geophys. Res.*, *74*(5), 1275–1286, doi:10.1029/JA074i005p01275.
- Taylor, J. B. (1974), Relaxation of toroidal plasma and generation of reverse magnetic fields, *Phys. Rev. Lett.*, *33*(19), 1139–1141.
- Ulusen, D., D. A. Brain, and D. L. Mitchell (2011), Observation of conical electron distributions over Martian crustal magnetic fields, *J. Geophys. Res.*, *116*, A07214, doi:10.1029/2010JA016217.
- Vignes, D., M. H. Acuña, J. E. P. Connerney, D. H. Crider, H. Rème, and C. Mazelle (2004), Magnetic flux ropes in the Martian atmosphere: Global characteristics, *Space Sci. Rev.*, *111*(1), 223–231.
- Woltjer, L. (1958), A theorem of force-free magnetic fields, *Proc. Natl. Acad. Sci. U. S. A.*, *44*(6), 489–491.